Suppressing surface and bulk effect enables high efficiency solution-processed kesterite solar cells

Yunhai Zhao, Jun Zhao, Xingye Chen, Michel Cathelinaud, Shuo Chen, Hongli Ma, Ping Fan, Xianghua Zhang, Zhenghua Su, Guangxing Liang

To cite this version:

Yunhai Zhao, Jun Zhao, Xingye Chen, Michel Cathelinaud, Shuo Chen, et al.. Suppressing surface and bulk effect enables high efficiency solution-processed kesterite solar cells. Chemical Engineering Journal, 2023, Chemical Engineering Journal, pp.147739. 10.1016/j.cej.2023.147739 . hal-04327518

HAL Id: hal-04327518
https://hal.science/hal-04327518v1

Submitted on 11 Sep 2024

Suppressing Surface and Bulk Effect enables High Efficiency Solution-Processed Kesterite Solar Cells

Yunhai Zhao[a,b], Jun Zhao[a,*], Xingye Chen[a], Michel Cathelinaud[b], Shuo Chen[a], Hongli Ma[b], Ping Fan[a], Xianghua Zhang[b], Zhenghua Su[a,*], Guangxing Liang[a,*]

[a]Shenzhen Key Laboratory of Advanced Thin Films and Applications Key Laboratory of Optoelectronic Devices and Systems, College of Physics and Optoelectronic Engineering, Shenzhen University, Shenzhen 518060, P. R. China.
E-mail: zhaojun@szu.edu.cn (Prof. Zhao), zhsu@szu.edu.cn (Prof. Su) and lgx@szu.edu.cn (Prof. Liang)

[b]CNRS, ISCR (Institut des Sciences Chimiques de Rennes), UMR 6226
Université de Rennes
Rennes F-35000, France

Abstract

Kesterite $Cu_2ZnSn(S,Se)_4$ (CZTSSe) is a promising photovoltaic material due to its environmentally friendly composition and excellent photovoltaic performance. Unfortunately, open-circuit voltage (Voc) deficit and insufficient fill factor (FF) due to the interface and bulk carrier recombination have become major obstacle to further improve the device performance. A new effective strategy is proposed to simultaneously improve the front interface and suppress the CZTSSe absorber defects by introducing a thin ammonium sulfide layer on the absorber surface by a pre-soaking and spin-coating-annealing method. Through this strategy, the absorber surface is optimized by adding S and removing the secondary phase. At the same time, the diffusion of S into the bulk transforms the dominant deep V_{Se} defect into shallower Cu_{Zn} defect, which effectively reduces carrier recombination in the CZTSSe bulk and at the CZTSSe/CdS interface, prolongs minority carrier lifetime, facilitates carrier collection, and reduces charge loss. The optimized sulfurization treatment significantly improves V_{OC} and FF to the point that device efficiency increases from 11.26% to 13.19%. These findings provide new insights into achieving higher efficiency in CZTSSe-based thin film solar cells by simultaneously optimizing the interface and bulk.

Keywords:

CZTSSe, solar cell, surface sulfurization, carrier transport enhancement, defects passivation

Introduction

The Earth's abundant reserves of kesterite $Cu_2ZnSn(S,Se)_4$ (CZTSSe) thin film has attracted extensive research interest in the last decade for the green non-toxicity and high-efficiency solar cells due to the high light absorption coefficient, tunable direct bandgap (E_g) and high quantum efficiency[1, 2]. However, as the most promising alternative to $Cu(In,Ga)Se_2$ (CIGS) solar cells, the power conversion efficiency (PCE) of CZTSSe (14.9%) is still far below the highest performance of CIGS solar cells (23.6%)[3]. Among the many factors constraining the improvement of device efficiency, carrier recombination at the heterojunction interface and the absorber bulk should be the key limiting factor. Interface and bulk defects leads to increased Shockley-Reed-Hall recombination (i.e., trap-assisted recombination), which inevitably results in larger open-circuit voltage deficit ($V_{OC\text{-}def}$)[4]. Meanwhile, a series of secondary phases are inevitably generated during the selenization process, which affects the attachment between the buffer layer and absorber and reduce the filling factor (FF)[5, 6]. Besides, the Sn(S,Se) is commonly used to suppress Sn loss at selenization progress, excess Sn(S,Se) may condense on absorber surface when it was cooling[7, 8]. The deep level defects in the absorber can be effectively passivated by cation (Ag, Cd, Ge, et al.) doping, and changing the selenization process to control the chemical environment during the crystallization process can also obtain absorber with lower defect density[9-11]. However, it is very difficult to improve the absorber bulk as well as the heterojunction interface properties by one strategy at the same time. It is necessary to find a way to solve both the defect and the interface problem to further increase the V_{OC} and FF. Electroactive defect reduction and secondary phase elimination at the

CZTSSe/CdS interface by surface treatment is an effective way to improve the quality of the heterojunction interface[6, 12].

Among the various guiding interface treatment strategy, sulfurization of the CZTSSe absorber has proven to be a simple and effective method[13, 14]. It consists of two main approaches: sulfur-containing vapor treatment and solution treatment. Post-annealing treatment at elevated temperatures under H_2S gas or S vapor atmosphere can effectively increase the V_{OC}, and the increase is usually attributed to the activation energy transfer of the interface state at the CZTSSe/CdS interface[15, 16]. In this case, the electron transport barrier formed on the surface of the S-rich component deteriorates the device efficiency, so it is essential to control the additional sulfur content introduced by the sulfurization treatment[17]. However, it is very difficult to accurately regulate sulfur doping in CZTSSe film during sulfurization treatment because of the high activity of sulfur at high temperature. Besides, due to the decomposition of kesterite film at high temperatures, elements such as Sn are easily lost. Sulfur-containing solution soaking, such as $(NH_4)_2S$ and Na_2S treatments could take out the secondary phase on the absorber surface and improve the surface wettability of absorber[7, 18]. However, the appropriate treatment time is crucial for the solution sulfurization treatment, and the absorber needs to be washed immediately after the treatment. The sulfurization activity is closely related to the reaction temperature, which makes it difficult to achieve the passivation of defects by this method. In order to achieve an effective sulfurization effect and at the same time a good control of the degree of sulfurization, a new sulfurization process needs to be explored.

In the present contribution, we report on an effective and simple solution treatment method that can be applied on the surface of sulfur-based thin films and achieve vapor sulfurization, being able to adjust simultaneously the surface property as well as the internal defect of the absorber. This method is based on the use of vapor from ammonium sulphide ($(NH_4)_2S$, abbreviated here AS) as a sulfur source. AS is a salt of a weak alkali and a weak acid and thermally decomposes at 280 ℃ to release H_2S as follows[19, 20],

$(NH_4)_2S \leftrightharpoons NH_3+H_2S$

compare with the solution soaking sulfurization process alone, the H_2S released at 280 ℃ is expected to obtain higher reactivity, while the benign treatment temperature of 280 ℃ promotes the diffusion of S elements, which can effectively passivate the interface defects as well as bulk defects. Therefore, AS sulfurization treatment is expected to suppress interface and bulk recombination synergistically and well control the elemental distribution, thus further improving the heterojunction quality and device performance.

Here, we provide an effective surface sulfurization method to optimize CZTSSe surface and passivate interface and bulk defect. The AS solution was coated on the CZTSSe absorber and stayed for 2 min, then spinning was performed to obtain thin AS layer on the absorber surface, finally sintered at 280 ℃ under inert atmosphere. The synergistic effect of surface etching and surface sulfurization can be obtained simultaneously by this method. After the surface sulfurization treatment, the sulfur content of absorber was slightly increased, carrier separation efficiency was enhanced and the carrier recombination was suppressed. This combined factors of enhanced charge transport capacity, reduced carrier recombination and extended carrier lifetime resulted in a significant increase in V_{OC} and FF and a device efficiency of 13.19% (the total-area efficiency is 12.71%).

Experiment

Preparation of CZTS precursor solution: The molar ratio of Cu/(Zn+Sn) and Zn/Sn were 0.775 and 1.2, respectively, and the solutions were prepared in air. Sn^{4+} solution was obtained by dissolving CuCl, $Zn(CH_3COO)_2 \cdot 2H_2O$, $SnCl_4 \cdot 5H_2O$ and $SC(NH_2)_2$ in 2-Methoxyethanol. Sn^{2+} solution was prepared by dissolving $Cu(CH_3COO)_2 \cdot H_2O$, $ZnCl_2$, $SnCl_2 \cdot 2H_2O$ and $SC(NH_2)_2$ in 2-Methoxyethanol. The Sn^{4+} and Sn^{2+} solution were mixed homogeneously in the same volume and then diluted to half of the original concentration to obtain the CZTS precursor solution.

Preparation of CZTSSe absorber: The CZTS precursor solution was spin-coated Mo substrate. The rotational speed was 3000 rmp and the film was annealed in a hot plate at 280 ℃ after spin-coating. This spin-coating and annealing cycle was repeated 10 times. Finally, the prepared CZTS precursor film were seleniated in a rapid thermal processing (RTP) furnace at 555 ℃, 900 s, and under argon flow to obtain CZTSSe absorber.

Sulfurization treatment: Method A: Soak the CZTSSe absorber in ammonium sulphide solution, use a stopwatch to accurately calculate the soaking time, and rinse the film with deionised water immediately after the soaking. The rinsed film was dried in an oven at 60 ℃. Method B: Place the CZTSSe absorber in the spin coater machine and use a dropper to draw ammonium sulphide solution onto the absorber surface so that the surface is completely covered by the ammonium sulphide solution. The infiltration time was accurately calculated using a stopwatch, and the spin coater machine was started immediately after the timing to rotate the film. The CZTSSe absorber covered with AS layer were then annealed on a hot plate at 280 °C. The same spin-coating parameters were used for the CTZS film and the AS layer. The solution was spin-coated with 3000 rpm for 20 s. The whole process was carried out in a glove box under nitrogen atmosphere.

Device preparation: The CdS buffer layer was prepared by chemical bath deposition on absorber. The ITO window layer was sputtered by magnetron sputtering on the buffer layer. Ag electrodes were deposited by thermal evaporation.

Characterizations: The X-ray diffraction (XRD) pattern was measured by Bruker AXS (D8 Advance). The surface topography and Mapping of the films were obtained using scanning electron microscopy (BRUKER QUANTAX 200). The current density-voltage (*J*-*V*) characteristics were represented by a Keithley 2400 multi-meter. The external quantum efficiency (EQE) spectrum were collected by Zolix SCS101 system and Keithley 2400 source meter. Ultraviolet photoelectron spectroscopy (UPS) were obtained by PHI 5000 VersaProbe III with He I source (21.22 eV). The X-ray photoelectron spectroscopy (XPS) was measured by PHI 5000 VersaProbe III with a monochromatic Al Kα X-ray source. The topography and surface potential were measured by Kelvin Electrostatic Force Microscopy (KPFM, Dimension Icon, Bruker).

Electrochemistry impedance spectroscopy (EIS) was measured by frequency response analysis (FRA) equipped PGSTAT-30 from Autolab (AUT302N). Temperature-dependent dark *J*-*V* (*J*-*V*-*T*) measurement were carried out using a Lakeshore 325 temperature controller. The transient photovoltage (TPV) spectra were collected by Agilent B1500A semiconductor characterization system. Admittance spectral measurement was collected through Lakeshore 325 temperature controller and the devices were mounted inside a Janis VPF-100 cryostat and the system was cooled with liquid nitrogen. Capacitance-voltage (*CV*) and drive-level capacitance spectroscopy (DLCP) were analysed by Keithley 4200A-SCS system with JANIS cryogenic platform. The device was put into a SEM vacuum chamber to implement EBIC measurements (Gatan, Inc.).

Results and Discussion.

Figure 1a demonstrates the preparation of CZTSSe thin films treated by AS solution sulfurization. The conventional AS solution sulfurization method usually selects a suitable soaking time to soak the CZTSSe absorber in AS solution at room temperature, and then the film are placed in deionized water, and finally dried it to obtain the treated film. The film prepared by the traditional method is called as sample A. The soaking time of AS solution corresponding to sample A1 and A2 is 1 and 2 min, respectively. Such a treatment removes secondary phase and passivates the defect of the absorber surface to some extent. Overall, this method is convenient but cannot improve the internal property (e.g., bulk defect) of the absorber, and thus the improvement of PCE is limited. Therefore, we chose a new treatment method: firstly, drop the AS solution on the CZTSSe absorber surface, so that the AS solution completely covers the whole film surface, stay for a few minutes to remove the secondary phase of the surface. Then turn on the spin coater machine, high-speed rotation makes the AS solution transformed into a thin AS layer[6, 21, 22]. Finally the sample are placed on a hot plate at 280 ℃ for annealing, the whole process was carried out in a glove box. The samples prepared using this method are called sample B, and the AS solution infiltration time of sample B1, B2 and B3 correspond to 1, 2 and 3 min, respectively. The H_2S released from the decomposition of AS at 280 ℃ has higher reactivity, and the favorable sulfurization temperature of 280 ℃ is conducive to promoting the diffusion of S into the interior of the absorber, which can effectively passivate the defect on the surface as well as in the bulk.

The XRD spectra and partial magnification of the reference sample and samples A, B are shown in Figure 1b and c, respectively. The XRD spectra indicate that the crystal structure of the samples is kesterite CZTSSe, and the bulge located on the right side of the (112) peak is assigned to the secondary phase Sn(S, Se)[7, 23]. The Sn(S, Se) peak intensity of the thin film treated with AS solution was significantly weakened than reference (Figure 1c), indicating that the secondary phase in the absorber was effectively removed. Moreover, the Sn(S,Se) peak intensity of A2 sample is lower than that of A1, and the Sn(S,Se) peak intensity of B1, B2 and B3 are weakened in turn, which means that the longer the AS solution stays on the absorber, the better the remove effect of the secondary phase is.

To investigate the effect of AS solution treatment on the device efficiency, the PCE of the reference sample and sample A, B are demonstrated in **Table 1**. The results show a negligible slight enhancement in short-circuit current density (J_{SC}) and V_{OC} and a small increase in FF, hence a slight enhancement in efficiency for the sample treated by method A. AS solution soaking removes the secondary phase of absorber surface, which favors better heterojunction quality, and therefore the FF is enhanced. The increase in V_{OC} and FF in the samples treated with method B was quite significant. Residence of the AS solution on the surface of the absorber dissolves the secondary phase, and subsequent rotation of the spin coater machine removes the secondary phase dissolved in the AS solution. Annealing at 280 ℃ in an inert gas atmosphere enhances the reactivity of the sulfurization and promotes elemental diffusion, and the AS decomposes into NH_3 and H_2S, which effectively passivates the electroactive defects on the surface and in the bulk of the absorber. The improvement of the heterojunction quality and the reduction of the defect lead to the enhancement of the FF and the V_{OC}, which resulted in an efficiency of 13.19%. The 2 minutes residence time of AS solution gives the best result.

In the following, the reference device and the optimal device B2 will be referred to as W/O AS and With AS respectively for ease of expression. **Figure 2**a illustrates the box statistics of the PV parameters, where the average efficiency of the With AS device increases from 11.15% to 12.76%. The enhancement of J_{SC} may originate from the reduction of recombination loss at the heterojunction interface and the enhancement of charge carrier collection[24]. SEM mapping test were performed on the surface of W/O

AS and With AS absorber to investigate the effect of AS treatment on the elemental content of the absorber surface, and the result is displayed in Figure 2b, c. The S content of With AS absorber surface increases obviously, the Se content changes insignificantly, and the Sn content decreases slightly, which coincides with the result that the Sn-related secondary phases are removed after the sulfurization treatment.

The EDS elemental line scan shows a slight increase of S content in the near-surface region (400 nm) of the absorber after sulfurization treatment (**Figure 3**a). Figure 3b demonstrates the changes of S/Se in the films before and after the sulfurization treatment and the corresponding bandgap changes, and the calculation of the bandgap based on S/Se is shown in the Supporting Information (**Note1**). With AS films possessing a larger value of S/Se near the surface, the surface bandgap is larger than that of the W/O AS films. The V_{OC} is proportional to the bandgap, and a slightly larger bandgap at the surface favors the enhancement of the V_{OC}. XPS is very sensitive to the elemental component of the sample surface, and the surface composition of the W/O AS and With AS CZTSSe absorber was investigated using XPS. Figure 3c illustrates the S 2p peak of both sample. Four peaks were observed in the S 2p spectra, the peaks at 161.0 and 162.2 eV belonged to the S 2p core, consistent with the sulphide state S located at 160-164 eV, while the peak at 159.7 and 165.4 eV belonged to the Se 3p core[25, 26]. The sulfurization treatment greatly affects the surface S peak intensity, the S peak intensity of the treated film surface is significantly increased compared to W/O AS film, which implied that the surface of the treated film had a higher S content. It is in agreement with the results of SEM-Mapping. Figure 3d shows the J-V curves of the

W/O AS and With AS device. The V_{OC} and FF of the With AS device demonstrates a significant enhancement, which may originate from the passivation of defects and the enhancement of bandgap. **Figure S1** shows the J-V curves for the light and dark states of the W/O AS and With AS device, and the series resistance (R_s), shunt resistance (R_{sh}), ideality factor (A), and reverse saturation current (J_0) calculated from the J-V curves are summarized in **Table 2**[27, 28]. The diode parameters (**Figure S2** and **Figure S3**) of the solar cell help us to analyze the performance loss mechanism of the device. With AS device have smaller R_s and larger R_{sh}, which is beneficial to enhance the FF. The A and J_0 of With AS devices are 1.5 and 1.57×10^{-5} mA cm^{-2}, respectively, which are smaller than that of the W/O AS devices[29, 30]. It implies that there is a significant reduction of carrier recombination in the With AS devices, which could be due to the sulfurization treatment passivation defects thereby reducing the number of carrier recombination centers.

The EQE curve are shown in Figure 3e. Consistent with J_{SC}, the AS sulfurization treatment slightly improves the EQE in the broad spectral range of 400-1000 nm, presumably due to the sulfurization treatment passivating the recombination center in the absorber and enhancing the carrier collection efficiency[12, 31]. Notably, the EQE response of the treated devices starts to decrease around 1000 nm, which is related to the decrease in long-wavelength absorption due to the S content increase in the absorber of the processed device[32]. The bandgap (E_g) was determined from EQE curve by linear extrapolation of $(\ln(1\text{-EQE}))^2$ versus wavelength (**Figure S4**)[33]. The E_g of the W/O AS and With AS device are 1.14 eV and 1.15 eV, respectively, and the E_g of the treated device increases slightly due to the increase in S content[34]. The integral current density calculated from the EQE spectral response is displayed in **Figure S5**. The integral current density of the W/O AS and With AS devices are 34.68 and 34.95 mA cm^{-2}, respectively, which are in good agreement with the J_{SC} in the *J-V* curves. The UPS analysis can obtain the work function and valence band of the semiconductor materials, which can be combined with the bandgap values to obtain the band alignment of the heterojunctions[35]. The UPS curves of CdS, W/O AS film and With AS film are shown in **Figures S5** and **S6**, respectively, and the calculation process of the work function is shown in the supporting information (**Note2**). The calculation results show that the conduction band of CdS is higher than that of W/O AS film and With AS film (the band alignment schematic is shown in Figure 3f), which proves that the p-n junctions of both devices are spike structures that are favorable for carrier transport (Supporting information **Note3**). The conduction band offset (CBO) of the heterojunction is 0.04 eV for the W/O AS device and 0.16 eV for the With AS device. The slightly increased CBO of the With AS device is more conducive to the reduction of interface recombination and does not affect the electron tunneling, which improves the performance of the device.

AFM and KPFM measurements are widely used in solar cells to analysis the spatial morphology and the potential distribution around the grain boundary (GB) of the samples. The 2D morphology and surface potential maps of the CZTSSe absorber are shown in **Figure 4**. The surface morphology of the two samples is in good agreement with the SEM images. The surface potentials of the W/O AS and With AS sample are shown in Figure 4b and e. The brightness of the grain boundary of the two samples is significantly higher than that of the grain interior (GI), which means that the contact potential difference (CPD) of the grain boundary are higher than grain interior. Higher CPDs at grain boundary lead to downward bending of the bands, which attracts electrons and repels holes[12, 36]. This downward bending phenomenon can promote the separation of electrons and holes, leading to a reduction in carrier recombination and an enhancement of carrier separation. In addition, the average potential difference of W/O AS and With As samples between the GB and GI is 26 and 73 mV, respectively (Figure 4g and Figure 4h, Supporting information **Note4**). It suggests that the AS sulfurization treatment increases the band bending at the grain boundary[37]. Larger band bending facilitates enhanced carrier separation and collection at grain boundary, suggesting that the higher carrier separation efficiency after surface sulfurization treatment is one of the reasons for the increase in V_{OC}.

The PCE of kesterite devices is limited by the level of deep traps at the interface and in the absorber bulk. Since annealing of the treated devices at 280 °C leads to ion exchange between the CZTSSe and AS layer, the defect property of the absorber may change accordingly. In order to gain insight into the correlation between interdiffusion and deep-trap states, we performed admittance spectral measurements on W/O AS devices and With AS devices. The admittance spectral results are shown in **Figure 5**a, c, the capacitance of the W/O AS device varies greatly with frequency, while the capacitance of the With AS content device varies less between high and low frequency. The significant frequency dependence of the capacitance in the W/O AS device suggests that there are greater density of traps in the absorber[32, 38]. Figure 5b and e shows the Arrhenius plots of the W/O AS and With AS device, the activation energy (E_a) determined from the Arrhenius plots approximates the difference between the defect level and the edge of the valence band (Supporting information **Note5** and **Figure S8**)[39, 40]. The E_a for the W/O AS and the With AS device is about 308 meV and 147 meV, respectively. A larger E_a value usually indicates a slower hole emission rate, so defects with larger activation energy are more likely to become more efficient recombination centers[32]. In the CZTSSe, the deeper energy level that are located at about 300 meV above the valence band defects include the acceptor defect Cu_{Sn} and the donor defect V_{Se}, while another defect level 150 meV away from the valence band can be attributed to the Cu_{zn} defect[5]. For the With AS devices, the annealing at 280 ℃ promotes ion exchange, and the S elements in the AS layer can diffuse into the absorber to a greater extent, which can passivate the V_{Se} defect on the absorber surface as well as in the bulk at the same time[6, 41]. Therefore, the dominant deep-energy level defects in the With AS device are converted from V_{Se} to Cu_{Zn}, which is the main reason for the V_{OC} enhancement in the With AS device. In contrast to V_{Se}, which deteriorates the device performance by trapping carriers as a deep energy level recombination center, ionization of the acceptor defect Cu_{Zn} generates a large number of hole carriers and leads to a good p-type conductivity[42].

Temperature-dependent *J-V* tests (*J-V-T*) are widely used to analyze carrier transport mechanism in thin-film solar cells. **Figure S9** shows the *J-V-T* curves of W/O AS and With AS devices from 120 k to 300 k under dark conditions. The diode-like behavior of the W/O AS device is largely suppressed at 220 k, whereas the *J*-*V* curves of the With AS device show good diode characteristics even when the temperature drops to 160 K, proving that the With AS device has a low transport barrier[43]. The reverse saturation current (J_0) and ideal factor (A) were extracted from the J-V curves. The A of the With AS device showed lower temperature dependence, indicating the dominance of Shockley-Read-Hall recombination in the depletion region (**Figure 6**a). The A of the W/O AS device was much larger and strongly correlated with the temperature, suggesting that unfavorable tunneling-enhanced recombination was dominant[44]. The dominant recombination paths can be found by plotting Aln(J_0) against 1/k*T* and calculating the slope E_A (Interface recombination activation energy, Figure 6b). E_A close to E_g indicates that bulk recombination dominates; whereas E_A less than E_g implies that interface recombination is dominant[44, 45]. The E_A of the W/O AS and With AS devices are 0.79 eV and 0.95 eV, respectively. The E_A values of With AS devices are close to the bandgap, indicating that the AS sulfurization treatment significantly passivates the interface recombination.

The carrier concentration of absorber and recombination property of heterojunction were investigated by *CV* and DLCP. Figure 6c is the *CV* and DLCP data for the W/O AS and the With AS device. The carrier density (N_{CV} amd N_{DL}) and the width of depletion region (W_d) derived from the DLCP data are shown in **Table 3**. The W_d is similar for both samples, but that the carrier density (zero bias) is larger for the With AS device. The carrier density of With AS device increases from 5.40×10^{16} to 6.66×10^{16} cm^3, which is attributed to the transformation of the dominant defect from V_{Se} to

Cu_{Zn}. In general, DLCP was only includes bulk defects, the *CV* was also includes interface defects[29, 46]. Therefore, the interface defect density (N_{IT}) can be obtained by comparing N_{CV}-N_{DLCP}. The N_{IT} value estimated for the W/O AS and With AS device were 3.34×10^{16} and 4.70×10^{15} cm^{-3}, respectively. The interface defects were reduced by an order of magnitude after the sulfurization treatment. Such a considerable decrease in N_{IT} strongly confirms the superiority of the heterojunction interface of With AS devices, which reduces the carrier recombination of heterojunction and accelerates the carrier transport at the interface[39, 47]. The carrier transport characteristics of the devices were analyzed by EIS, and the correlation curves and fitting results are displayed in **Figure S10** and Table 3. The inset of Figure S10 shows the equivalent circuit diagram of the CZTSSe solar cell, and the EIS curves were fitted to obtain the series resistance (R_s*), recombination resistance (R_{rec}), and chemical capacitance (C_{rec}). The smaller R_s* and larger R_{rec} of the AS devices imply that carrier recombination in the devices is effectively suppressed[48, 49]. According to the diffusion-recombination model, the minority carrier lifetimes (τ) of 0.59 and 2.33 microseconds for the two devices, indicating that the sulfurization treatment significantly improves the carrier transport dynamics of the devices.

To further evaluate the carrier lifetime in fully working devices, the W/O AS and With AS device were tested for TPV, where photocarriers are generated under pulsed light irradiation, free electrons and holes are produced and a photovoltage is generated. Once the incident light is switched off, the voltage starts to decay due to transient non-radiative recombination of electrons and holes at possible defect locations[2, 50].

Figure 6d shows the TPV results for the W/O AS and the With AS device. Based on the results of the single-exponential model fitting, it is found that the TPV lifetime (τ_{TPV}) of the With AS device increases from 10.38 μs to 12.89 μs. The longer decay time provides more opportunity for carriers to be extracted from the absorber to the electrodes, which greatly reduces the carrier recombination. We know that a relatively long decay time means fewer non-radiative recombination sites in the intact device. Therefore, the AS sulfurization treatment reduces the defects in the CZTSSe, which reduces the recombination of free carriers and facilitates carrier collection and cell performance.

The improvement in charge transport induced by sulfurization-enhanced carrier collection and separation at grain boundary may be the direct cause of the enhanced electrical property of the devices. EBIC can help us to further investigate the transport of electrons across grain boundary at microscopic level. The SEM cross-section, EBIC mapping is shown in Figure 6e, f, Figure 6g shows the normalized EBIC signals of the W/O AS and With AS device along the grey dashed line. Bright regions in the EBIC image imply high carrier collection efficiency, and the depths represent minority carrier diffusion lengths[51, 52]. Near the CdS/CZTSSe interface, both samples show strong carrier collection, and the reason for the strong EBIC signal near the interface is the strong electric field in the region. It indicates high carrier collection efficiency near the heterojunction. The EBIC signal is significantly weaker away from the p-n junction, which was limited by the possible presence of significant recombination and/or carrier transport barriers. Compared to W/O AS device. With AS device have stronger EBIC signal at the heterojunction interface (**Figure S11**, non-normalized EBIC line scan), implying that With AS device have stronger built-in electric field, as reflected in the KPFM data[53, 54]. Meanwhile, the EBIC signal of the With AS device decreases slower and has higher intensity near the back interface (Figure 6g, normalized EBIC line scan), indicating that the AS sulfurization treatment effectively improves the carrier collection capability, the carrier diffusion length is extended and the charge collection process is improved.

Conclusion

This manuscript proposes a simple and effective method to simultaneously treat surface and bulk of CZTSSe device by a pre-soaking and spin-coating-annealing sulfurization for the first time. The champion CZTSSe device based on the optimal AS solution sulfurization treatment duration obtain PCE of 13.19%. This strategy adds an annealing step to the surface sulfurization process, which promotes elemental diffusion and passivates surface and bulk defects of CZTSSe devices. The removal of secondary phase from the absorber surface facilitates better p-n junction quality and reduces interface carrier recombination. Further study shows that the band bending at grain boundary of the treated samples is larger, which is more favorable for the carrier separation and collection ability. The conversion of the dominant deep energy level defect from V_{Se} to Cu_{Zn} reduces the recombination of free carriers. Stronger EBIC signals and slower decay rates indicate that the AS sulfurization treatment effectively improves the carrier collection, extends the carrier diffusion length and improves the charge collection process. The present work provides a new idea and easy-to-handle method for removing the bulk defects and the front interface of the secondary phase-time-modified high-efficiency kesterite solar cells on the absorber layer surface.

Declaration of Competing Interest

The authors declare no conflict of interest.

Acknowledgments

This work was supported by the National Natural Science Foundation of China (No. 62074102), Guangdong Basic and Applied Basic Research Foundation (2022A1515010979) China, Science and Technology plan project of Shenzhen (20220808165025003) China.

Reference

[1] J. Zhou, X. Xu, H. Wu, J. Wang, L. Lou, K. Yin, Y. Gong, J. Shi, Y. Luo, D. Li, H. Xin, Q. Meng, Control of the phase evolution of kesterite by tuning of the selenium partial pressure for solar cells with 13.8% certified efficiency, Nat. Energy 8(5) (2023) 526-535, https://doi.org/10.1038/s41560-023-01251-6.

[2] Y.-H. Zhao, Q.-Q. Gao, S.-J. Yuan, Q.-Q. Chang, T. Liang, Z.-H. Su, H.-L. Ma, S. Chen, G.-X. Liang, P. Fan, X.-H. Zhang, S.-X. Wu, Defects passivation and crystal growth promotion by solution-processed K doping strategy toward 16.02% efficiency Cu(In,Ga)(S,Se)$_2$ solar cells, Chem. Eng. J. 436 (2022) 135008, https://doi.org/10.1016/j.cej.2022.135008.

[3] M.A. Green, E.D. Dunlop, M. Yoshita, N. Kopidakis, K. Bothe, G. Siefer, X. Hao, Solar cell efficiency tables (version 62), Prog. Photovolt: Res. Appl. 31(7) (2023) 651-663, https://doi.org/10.1002/pip.3726.

[4] L. Lou, Y. Gong, J. Zhou, J. Wang, X. Xu, K. Yin, B. Duan, H. Wu, J. Shi, Y. Luo, D. Li, H. Xin, Q. Meng, A feasible and effective solution-processed PCBM electron extraction layer enabling the high V_{OC} and efficient Cu$_2$ZnSn(S, Se)$_4$ devices, J. Energy Chem. 70 (2022) 154-161, https://doi.org/10.1016/j.jechem.2022.02.009.

[5] S. Chen, A. Walsh, X.G. Gong, S.H. Wei, Classification of lattice defects in the kesterite Cu$_2$ZnSnS$_4$ and Cu$_2$ZnSnSe$_4$ earth-abundant solar cell absorbers, Adv. Mater. 25(11) (2013) 1522-39, https://doi.org/10.1002/adma.201203146.

[6] M. Buffière, A.-A.E. Mel, N. Lenaers, G. Brammertz, A.E. Zaghi, M. Meuris, J.

Poortmans, Surface Cleaning and Passivation Using $(NH_4)_2S$ Treatment for $Cu(In,Ga)Se_2$ Solar Cells: A Safe Alternative to KCN, Adv. Energy Mater. 5(6) (2015) 1401689, https://doi.org/10.1002/aenm.201401689.

[7] H. Xie, Y. Sanchez, S. Lopez-Marino, M. Espindola-Rodriguez, M. Neuschitzer, D. Sylla, A. Fairbrother, V. Izquierdo-Roca, A. Perez-Rodriguez, E. Saucedo, Impact of Sn(S,Se) secondary phases in $Cu_2ZnSn(S,Se)_4$ solar cells: a chemical route for their selective removal and absorber surface passivation, ACS Appl. Mater. Interfaces 6(15) (2014) 12744-51, https://doi.org/10.1021/am502609c.

[8] M. Buffiere, G. Brammertz, S. Sahayaraj, M. Batuk, S. Khelifi, D. Mangin, A.A. El Mel, L. Arzel, J. Hadermann, M. Meuris, J. Poortmans, KCN Chemical Etch for Interface Engineering in $Cu_2ZnSnSe_4$ Solar Cells, ACS Appl. Mater. Interfaces 7(27) (2015) 14690-8, https://doi.org/10.1021/acsami.5b02122.

[9] Y. Gong, R. Qiu, C. Niu, J. Fu, E. Jedlicka, R. Giridharagopal, Q. Zhu, Y. Zhou, W. Yan, S. Yu, J. Jiang, S. Wu, D.S. Ginger, W. Huang, H. Xin, Ag incorporation with controlled grain growth enables 12.5% efficient kesterite solar cell with open circuit voltage reached 64.2% shockley–queisser limit, Adv. Funct. Mater. 31(24) (2021) 2101927, https://doi.org/10.1002/adfm.202101927.

[10] J. Wang, J. Zhou, X. Xu, F. Meng, C. Xiang, L. Lou, K. Yin, B. Duan, H. Wu, J. Shi, Y. Luo, D. Li, H. Xin, Q. Meng, Ge bidirectional diffusion to simultaneously engineer back interface and bulk defects in the absorber for efficient CZTSSe solar cells, Adv. Mater. 34(27) (2022) e2202858, https://doi.org/10.1002/adma.202202858.

[11] M. He, J. Huang, J. Li, J.S. Jang, U.P. Suryawanshi, C. Yan, K. Sun, J. Cong, Y. Zhang, H. Kampwerth, M.P. Suryawanshi, J. Kim, M.A. Green, X. Hao, Systematic efficiency improvement for $Cu_2ZnSn(S,Se)_4$ solar cells by double cation incorporation with Cd and Ge, Adv. Funct. Mater. 31(40) (2021) 2104528, https://doi.org/10.1002/adfm.202104528.

[12] S. Yuan, X. Wang, Y. Zhao, Q. Chang, Z. Xu, J. Kong, S. Wu, Solution Processed $Cu(In,Ga)(S,Se)_2$ Solar Cells with 15.25% Efficiency by Surface Sulfurization, ACS Appl. Energy Mater. 3(7) (2020) 6785-6792, https://doi.org/10.1021/acsaem.0c00917.

[13] W.C. Liu, B.L. Guo, X.S. Wu, F.M. Zhang, C.L. Mak, K.H. Wong, Facile hydrothermal synthesis of hydrotropic Cu_2ZnSnS_4 nanocrystal quantum dots: band-gap engineering and phonon confinement effect, J. Mater. Chem. A 1(9) (2013) 3182, https://doi.org/10.1039/c3ta00357d.

[14] L. Yu, X. Dong, F. Yang, X. Sun, J. Chen, X. Zhang, Y. Zhao, Y. Li, $(NH_4)_2S$-induced improvement of interfacial wettability for high-quality heterojunctions to boost the chloride-assembled CZTSSe solar cells, J. Chem. Phys. 157(13) (2022) 134706, https://doi.org/10.1063/5.0113110.

[15] J. Zhong, Z. Xia, M. Luo, J. Zhao, J. Chen, L. Wang, X. Liu, D.J. Xue, Y.B. Cheng, H. Song, J. Tang, Sulfurization induced surface constitution and its correlation to the performance of solution-processed $Cu_2ZnSn(S,Se)_4$ solar cells, Scientific reports 4 (2014) 6288, https://doi.org/10.1038/srep06288.

[16] T. Taskesen, D. Pareek, D. Hauschild, A. Haertel, L. Weinhardt, W. Yang, T.

Pfeiffelmann, D. Nowak, C. Heske, L. Gutay, Steep sulfur gradient in CZTSSe solar cells by H_2S-assisted rapid surface sulfurization, RSC Adv. 11(21) (2021) 12687-12695, https://doi.org/10.1039/d1ra00494h.

[17] K.-C. Wang, H.-R. Hsu, H.-S. Chen, Study of surface sulfurization of $Cu_2ZnSn(S, Se)_4$ thin film solar cell by sequential H_2Se-selenization/H_2S-sulfurization, Sol. Energy Mater. Sol. Cells 163 (2017) 31-37, https://doi.org/10.1016/j.solmat.2017.01.012.

[18] Z. Wei, M.J. Newman, W.C. Tsoi, T.M. Watson, Raman mapping analysis for removal of surface secondary phases of CZTS films using chemical etching, Appl. Phys. Lett. 109(12) (2016), https://doi.org/10.1063/1.4963134.

[19] Dae-Kwang Park, Young-Gu Cho, Dae-Won Park, H.-C. Woo, Kinetic Study on the Selective Oxidation of H_2S Containing Excess Water and Ammonia, React. Kinet. Catal. Lett. 74(1) (2001) 57-66.

[20] M. Buffière, T. Lepetit, S. Khelifi, A.-A. El Mel, Interface Engineering in $CuInSe_2$ Solar Cells Using Ammonium Sulfide Vapors, Solar RRL 1(6) (2017) 1700067, https://doi.org/10.1002/solr.201700067.

[21] M.E. Erkan, V. Chawla, I. Repins, M.A. Scarpulla, Interplay between surface preparation and device performance in CZTSSe solar cells: Effects of KCN and NH_4OH etching, Sol. Energy Mater. Sol. Cells 136 (2015) 78-85, https://doi.org/10.1016/j.solmat.2015.01.006.

[22] V. kumar, S. Padhy, A. Basak, U.P. Singh, Effect of HCl and NH_4OH etching on CZTSSe absorber layer, Vacuum 155 (2018) 336-338,

https://doi.org/10.1016/j.vacuum.2018.06.038.

[23] Y. Deng, Z. Zhou, X. Zhang, L. Cao, W. Zhou, D. Kou, Y. Qi, S. Yuan, Z. Zheng, S. Wu, Adjusting the Sn_{Zn} defects in $Cu_2ZnSn(S,Se)_4$ absorber layer via Ge^{4+} implanting for efficient kesterite solar cells, J. Energy Chem. 61 (2021) 1-7, https://doi.org/10.1016/j.jechem.2021.02.011.

[24] L. Yu, X. Dong, F. Yang, X. Sun, J. Chen, X. Zhang, Y. Zhao, Y. Li, (NH4)2S-induced improvement of interfacial wettability for high-quality heterojunctions to boost the chloride-assembled CZTSSe solar cells, J. Chem. Phys. 157(13) (2022) 134706, https://doi.org/10.1063/5.0113110.

[25] M. Danilson, M. Altosaar, M. Kauk, A. Katerski, J. Krustok, J. Raudoja, XPS study of CZTSSe monograin powders, Thin Solid Films 519(21) (2011) 7407-7411, https://doi.org/10.1016/j.tsf.2010.12.165.

[26] M. Kim, G.D. Park, Y.C. Kang, Investigation of the potassium-ion storage mechanism of nickel selenide materials and rational design of nickel selenide-C yolk-shell structure for enhancing electrochemical properties, Int. J. Energy Res. 46(5) (2021) 5800-5810, https://doi.org/10.1002/er.7523.

[27] Y. Luo, G. Chen, S. Chen, N. Ahmad, M. Azam, Z. Zheng, Z. Su, M. Cathelinaud, H. Ma, Z. Chen, P. Fan, X. Zhang, G. Liang, Carrier Transport Enhancement Mechanism in Highly Efficient Antimony Selenide Thin-Film Solar Cell, Adv. Funct. Mater. 33(14) (2023), https://doi.org/10.1002/adfm.202213941.

[28] P. Fan, J. Lin, J. Hu, Z. Yu, Y. Zhao, S. Chen, Z. Zheng, J. Luo, G. Liang, Z. Su, Over 10% efficient Cu_2CdSnS_4 solar cells fabricated from optimized sulfurization,

Adv. Funct. Mater. 32(45) (2022) 2207470, https://doi.org/10.1002/adfm.202207470.

[29] S. Chen, Y. Fu, M. Ishaq, C. Li, D. Ren, Z. Su, X. Qiao, P. Fan, G. Liang, J. Tang, Carrier recombination suppression and transport enhancement enable high-performance self-powered broadband Sb_2Se_3 photodetectors, InfoMat 5(4) (2023), https://doi.org/10.1002/inf2.12400.

[30] G. Liang, M. Chen, M. Ishaq, X. Li, R. Tang, Z. Zheng, Z. Su, P. Fan, X. Zhang, S. Chen, Crystal Growth Promotion and Defects Healing Enable Minimum Open-Circuit Voltage Deficit in Antimony Selenide Solar Cells, Adv. Sci. 9(9) (2022) e2105142, https://doi.org/10.1002/advs.202105142.

[31] Y. Zhao, S. Yuan, D. Kou, Z. Zhou, X. Wang, H. Xiao, Y. Deng, C. Cui, Q. Chang, S. Wu, High efficiency CIGS solar cells by bulk defect passivation through Ag substituting strategy, ACS Appl. Mater. Interfaces 12(11) (2020) 12717-12726, https://doi.org/10.1021/acsami.9b21354.

[32] H.-S. Duan, W. Yang, B. Bob, C.-J. Hsu, B. Lei, Y. Yang, The role of sulfur in solution-processed $Cu_2ZnSn(S,Se)_4$ and its Effect on defect properties, Adv. Funct. Mater. 23(11) (2013) 1466-1471, https://doi.org/10.1002/adfm.201201732.

[33] R. Tang, S. Chen, Z.H. Zheng, Z.H. Su, J.T. Luo, P. Fan, X.H. Zhang, J. Tang, G.X. Liang, Heterojunction Annealing Enabling Record Open-Circuit Voltage in Antimony Triselenide Solar Cells, Adv. Mater. 34(14) (2022) e2109078, https://doi.org/10.1002/adma.202109078.

[34] S.G. Haass, M. Diethelm, M. Werner, B. Bissig, Y.E. Romanyuk, A.N. Tiwari,

11.2% Efficient Solution Processed Kesterite Solar Cell with a Low Voltage Deficit, Adv. Energy Mater. 5(18) (2015) 1500712, https://doi.org/10.1002/aenm.201500712.

[35] T. Wu, J. Hu, S. Chen, Z. Zheng, M. Cathelinaud, H. Ma, Z. Su, P. Fan, X. Zhang, G. Liang, Energy Band Alignment by Solution-Processed Aluminum Doping Strategy toward Record Efficiency in Pulsed Laser-Deposited Kesterite Thin-Film Solar Cell, ACS Appl. Mater. Interfaces (2023), https://doi.org/10.1021/acsami.2c22174.

[36] Z. Yu, C. Li, S. Chen, Z. Zheng, P. Fan, Y. Li, M. Tan, C. Yan, X. Zhang, Z. Su, G. Liang, Unveiling the Selenization Reaction Mechanisms in Ambient Air-Processed Highly Efficient Kesterite Solar Cells, Adv. Energy Mater. 13(19) (2023) 2300521, https://doi.org/10.1002/aenm.202300521.

[37] J. Zhou, X. Xu, B. Duan, H. Wu, J. Shi, Y. Luo, D. Li, Q. Meng, Regulating crystal growth via organic lithium salt additive for efficient kesterite solar cells, Nano Energy 89 (2021) 106405, https://doi.org/10.1016/j.nanoen.2021.106405.

[38] Q. Cao, O. Gunawan, M. Copel, K.B. Reuter, S.J. Chey, V.R. Deline, D.B. Mitzi, Defects in Cu(In,Ga)Se_2 Chalcopyrite Semiconductors: A Comparative Study of Material Properties, Defect States, and Photovoltaic Performance, Adv. Energy Mate. 1(5) (2011) 845-853, https://doi.org/10.1002/aenm.201100344.

[39] R. Tang, Z.-H. Zheng, Z.-H. Su, X.-J. Li, Y.-D. Wei, X.-H. Zhang, Y.-Q. Fu, J.-T. Luo, P. Fan, G.-X. Liang, Highly efficient and stable planar heterojunction solar cell based on sputtered and post-selenized Sb_2Se_3 thin film, Nano Energy 64 (2019)

103929, https://doi.org/10.1016/j.nanoen.2019.103929.

[40] G. Liang, Z. Li, M. Ishaq, Z. Zheng, Z. Su, H. Ma, X. Zhang, P. Fan, S. Chen, Charge Separation Enhancement Enables Record Photocurrent Density in $Cu_2ZnSn(S,Se)_4$ Photocathodes for Efficient Solar Hydrogen Production, Adv. Energy Mater. 13(19) (2023), https://doi.org/10.1002/aenm.202300215.

[41] H. Jeong, R. Nandi, J.Y. Cho, P.S. Pawar, H.S. Lee, K.E. Neerugatti, J.H. Kim, J. Heo, CZTSSe/Zn(O,S) heterojunction solar cells with 9.82% efficiency enabled via $(NH_4)_2S$ treatment of absorber layer, Prog. Photovolt: Res. Appl. 29(10) (2021) 1057-1067, https://doi.org/10.1002/pip.3439.

[42] J. Li, Y. Huang, J. Huang, G. Liang, Y. Zhang, G. Rey, F. Guo, Z. Su, H. Zhu, L. Cai, K. Sun, Y. Sun, F. Liu, S. Chen, X. Hao, Y. Mai, M.A. Green, Defect control for 12.5% efficiency $Cu_2ZnSnSe_4$ kesterite thin-film solar cells by engineering of local chemical environment, Adv. Mater. 32(52) (2020) e2005268, https://doi.org/10.1002/adma.202005268.

[43] S. Siebentritt, E. Avancini, M. Bär, J. Bombsch, E. Bourgeois, S. Buecheler, R. Carron, C. Castro, S. Duguay, R. Félix, E. Handick, D. Hariskos, V. Havu, P. Jackson, H.P. Komsa, T. Kunze, M. Malitckaya, R. Menozzi, M. Nesladek, N. Nicoara, M. Puska, M. Raghuwanshi, P. Pareige, S. Sadewasser, G. Sozzi, A.N. Tiwari, S. Ueda, A. Vilalta-Clemente, T.P. Weiss, F. Werner, R.G. Wilks, W. Witte, M.H. Wolter, Heavy Alkali Treatment of $Cu(In,Ga)Se_2$ Solar Cells: Surface versus Bulk Effects, Adv. Energy Mater. 10(8) (2020) 1903752, https://doi.org/10.1002/aenm.201903752.

[44] B.L. Williams, S. Smit, B.J. Kniknie, K.J. Bakker, W. Keuning, W.M.M. Kessels, R.E.I. Schropp, M. Creatore, Identifying parasitic current pathways in CIGS solar cells by modelling dark J-V response, Prog. Photovoltaics 23(11) (2015) 1516-1525, https://doi.org/10.1002/pip.2582.

[45] G.S. Park, V.B. Chu, B.W. Kim, D.W. Kim, H.S. Oh, Y.J. Hwang, B.K. Min, Achieving 14.4% Alcohol-Based Solution-Processed $Cu(In,Ga)(S,Se)_2$ Thin Film Solar Cell through Interface Engineering, ACS Appl. Mater. Interfaces 10(12) (2018) 9894-9899, https://doi.org/10.1021/acsami.8b00526.

[46] Y. Zhao, S. Yuan, Q. Chang, Z. Zhou, D. Kou, W. Zhou, Y. Qi, S. Wu, Controllable Formation of Ordered Vacancy Compound for High Efficiency Solution Processed $Cu(In,Ga)Se_2$ Solar Cells, Adv. Funct. Mater. 31(10) (2020) 2007928, https://doi.org/10.1002/adfm.202007928.

[47] X.-Y. Chen, M. Ishaq, N. Ahmad, R. Tang, Z.-H. Zheng, J.-G. Hu, Z.-H. Su, P. Fan, G.-X. Liang, S. Chen, Ag, Ti dual-cation substitution in $Cu_2ZnSn(S,Se)_4$ induced growth promotion and defect suppression for high-efficiency solar cells, J. Mater. Chem. A 10(42) (2022) 22791-22802, https://doi.org/10.1039/d2ta05909f.

[48] M. Azam, Y.D. Luo, R. Tang, S. Chen, Z.H. Zheng, Z.H. Su, A. Hassan, P. Fan, H.L. Ma, T. Chen, G.X. Liang, X.H. Zhang, Organic Chloride Salt Interfacial Modified Crystallization for Efficient Antimony Selenosulfide Solar Cells, ACS Appl. Mater. Interfaces 14(3) (2022) 4276-4284, https://doi.org/10.1021/acsami.1c20779.

[49] N. Ahmad, Y. Zhao, F. Ye, J. Zhao, S. Chen, Z. Zheng, P. Fan, C. Yan, Y. Li, Z. Su,

X. Zhang, G. Liang, Cadmium-Free Kesterite Thin-Film Solar Cells with High Efficiency Approaching 12%, Adv. Sci. 10(26) (2023) e2302869, https://doi.org/10.1002/advs.202302869.

[50] Y. Li, L. Meng, Y.M. Yang, G. Xu, Z. Hong, Q. Chen, J. You, G. Li, Y. Yang, Y. Li, High-efficiency robust perovskite solar cells on ultrathin flexible substrates, Nat. Commun. 7 (2016) 10214, https://doi.org/10.1038/ncomms10214.

[51] W. Wang, M.T. Winkler, O. Gunawan, T. Gokmen, T.K. Todorov, Y. Zhu, D.B. Mitzi, Device characteristics of CZTSSe thin-film solar cells with 12.6% efficiency, Adv. Energy Mater. 4(7) (2014) 1301465, https://doi.org/10.1002/aenm.201301465.

[52] T. Ogihara, A. Sadono, T. Nishimura, K. Nakada, A. Yamada, Control of valence band offset of Cu(In,Ga)Se_2 solar cells with single-graded band profile, Jpn. J. Appl. Phys. 56(6) (2017) 062301, https://doi.org/10.7567/jjap.56.062301.

[53] X. Zhao, X. Chang, D. Kou, W. Zhou, Z. Zhou, Q. Tian, S. Yuan, Y. Qi, S. Wu, Lithium-assisted synergistic engineering of charge transport both in GBs and GI for Ag-substituted $Cu_2ZnSn(S,Se)_4$ solar cells, J. Energy Chem. 50 (2020) 9-15, https://doi.org/10.1016/j.jechem.2020.03.007.

[54] G.X. Liang, C.H. Li, J. Zhao, Y. Fu, Z.X. Yu, Z.H. Zheng, Z.H. Su, P. Fan, X.H. Zhang, J.T. Luo, L. Ding, S. Chen, Self-powered broadband kesterite photodetector with ultrahigh specific detectivity for weak light applications, SusMat 3(5) (2023) 682-696, https://doi.org/10.1002/sus2.160.

Table 1 Photovoltaic parameters of reference, A and B solar cells.

	REF	**A1**	**A2**	**B1**	**B2**	**B3**
J_{SC} (mA/cm^2)	37.27	37.82	37.54	37.34	37.47	37.35
V_{OC} (V)	0.494	0.493	0.495	0.510	0.531	0.514
FF (%)	63.10	63.29	63.74	64.37	66.30	65.55
PCE (%)	11.26	11.80	11.84	11.98	13.19	12.32

Table 2 Diode parameters, bandgap, defect recombination activation energy and deep defect density for W/O AS and With AS devices

	R_s (Ω)	**R_{sh} (Ω)**	**A**	**J_0 (mA cm^{-2})**	**E_g (eV)**	**E_a (meV)**	**N_T (cm^{-3})**
W/O AS	1.41	383	1.64	2.70×10^{-5}	1.14	308	3.10×10^{16}
With AS	0.71	441	1.50	1.57×10^{-5}	1.15	147	1.10×10^{16}

Table 3 Calculated results of *CV*, DLCP, EIS and TPV analysis.

	N_{CV} (cm^{-3})	**N_{DL} (cm^{-3})**	**W_d (μm)**	**N_{IT} (cm^{-3})**	**R_{rec} (Ω)**	**R_s* (Ω)**	**C_{rec} (nF)**	**τ (μs)**	**τ_{TPV} (μs)**
W/O AS	8.74×10^{16}	5.40×10^{16}	0.191	3.34×10^{16}	30.36	25.14	19.43	0.59	10.38
With AS	7.13×10^{16}	6.66×10^{16}	0.190	4.70×10^{15}	46.85	71.33	49.73	2.33	12.89

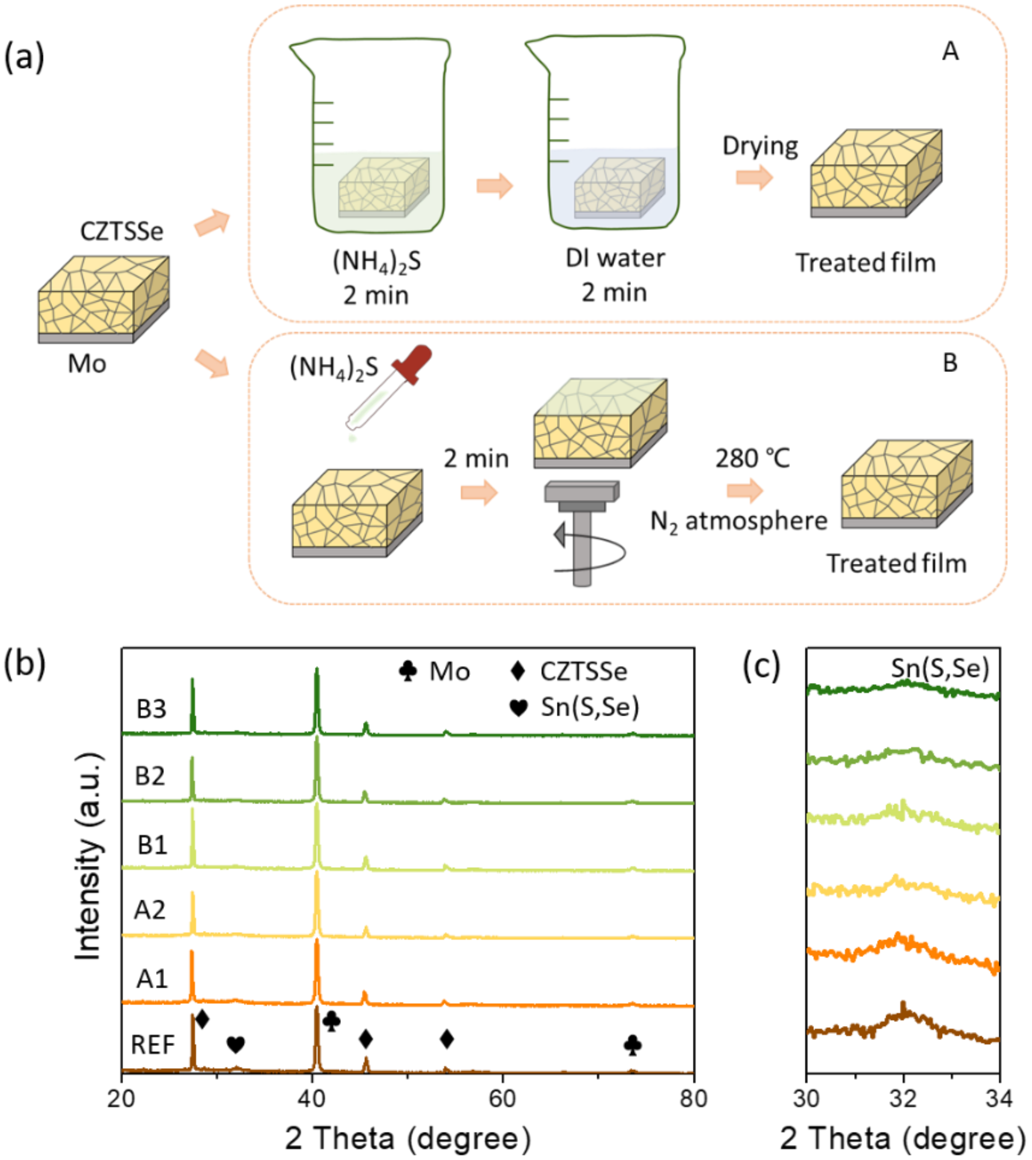

Figure 1 (a) Illustration of different AS sulfurization treatment processes, (b) XRD patterns of the reference sample, sample A and sample B, (c) The enlarged characteristic of (112) peak.

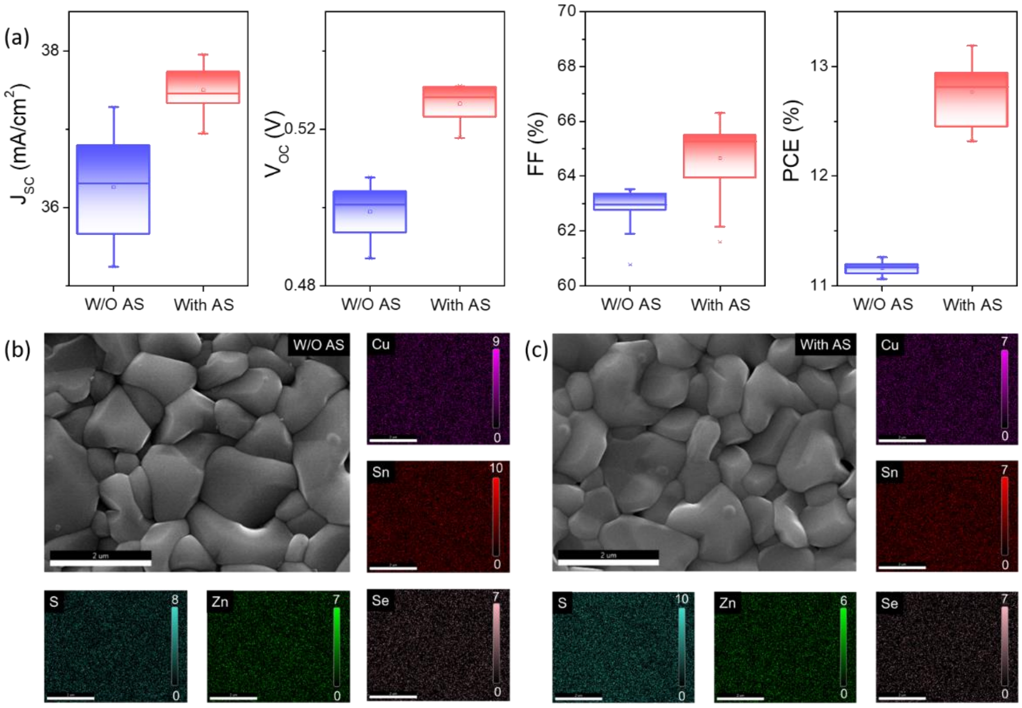

Figure 2 (a) Statistical boxplot of J_{SC}, V_{OC}, FF and PCE for W/O AS and With AS device, (b) SEM image and EDS mapping of the W/O AS film, (c) SEM image and EDS mapping of the With AS film.

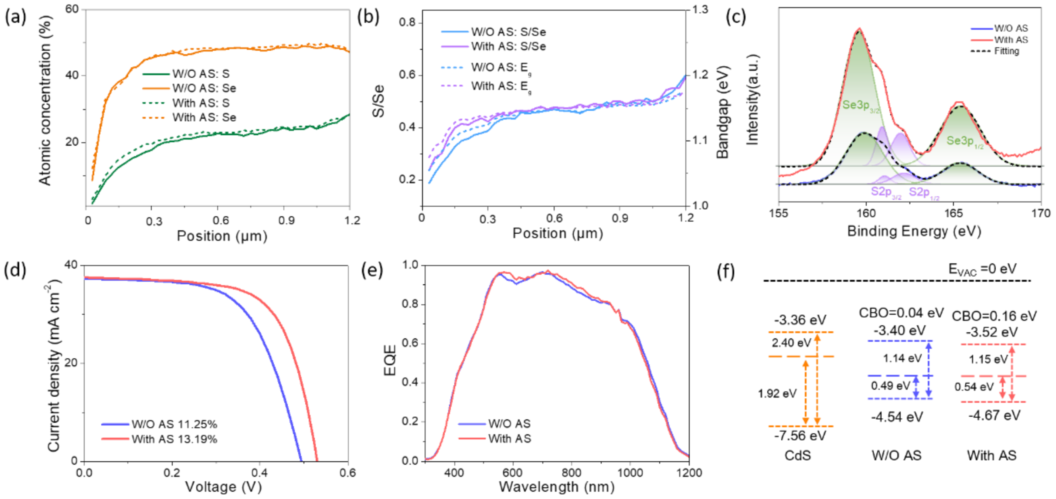

Figure 3 (a) S and Se elemental line scans of W/O AS and With AS films, (b) S/Se profiles and bandgap profiles of W/O AS and With AS films, (c) XPS analysis of S 3p for the W/O AS and With AS film, (d) *J*-*V* characteristics of CZTSSe device W/O AS and With AS, (e) EQE of W/O AS and With AS device, (f) heterojunction band alignment schematic for W/O AS and With AS devices.

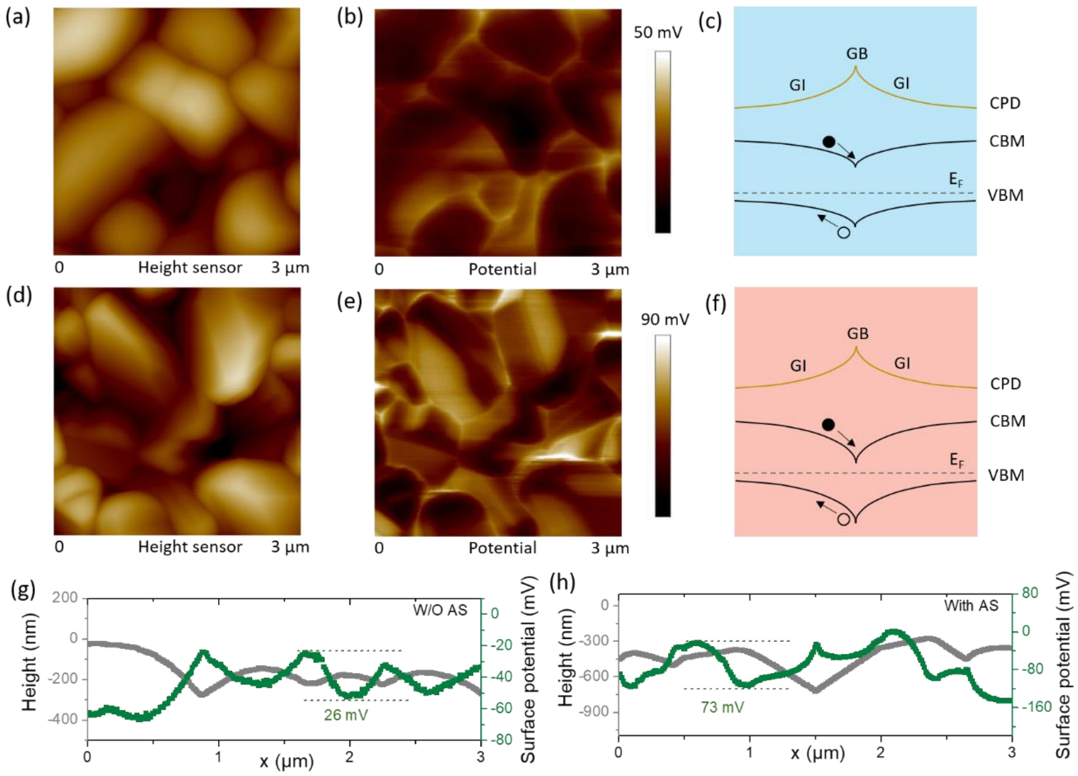

Figure 4 AFM and KPFM of the (a, b) W/O AS film and (d, e) With AS film. Schematic of the band diagram and CPD near grain boundary of (c) W/O AS film and (f) With AS film. The potential variation of (g) W/O AS film and (h) With AS film.

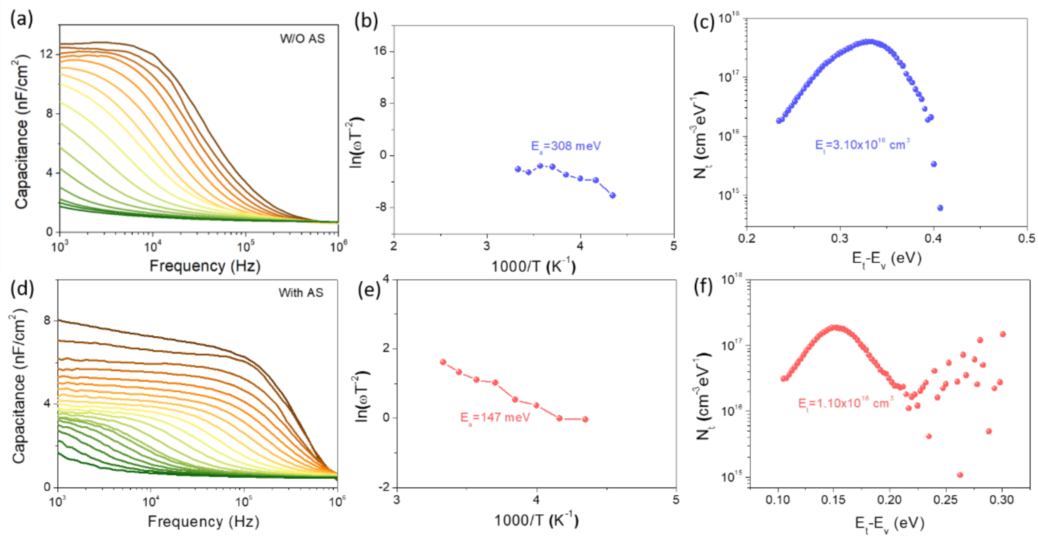

Figure 5 Admittance spectral results for (a) W/O AS, (d) With AS, from the inflection points of the *C*-*f*-*T* results, the Arrhenius plots of (b) W/O AS, (e) With AS, the defect density of states for (c) W/O AS, (f) With AS.

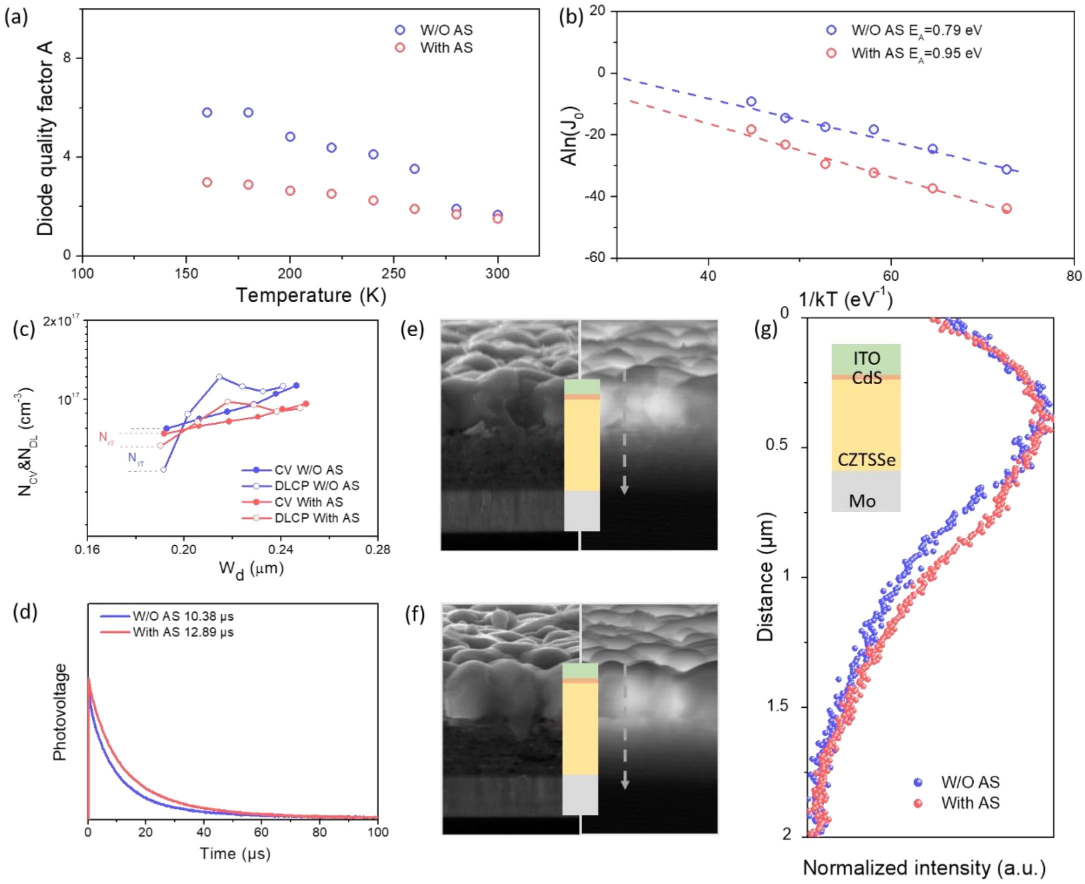

Figure 6 (a) Temperature dependence of ideal factor of W/O AS and With AS device, (b) Aln(J0) versus 1/kT plot of W/O AS and With AS device, (c) The plot of *CV* and DLCP for devices W/O AS and With AS, (d) TPV spectra of W/O AS and With AS device, cross-sectional SEM and EBIC images for (e) W/O AS device and (f) With AS device, (g) the intensity profiling of the dashed line in EBIC images.

Supporting information

Suppressing Surface and Bulk Effect enables High Efficiency Solution-Processed Kesterite Solar Cells

Yunhai Zhao[a,b], Jun Zhao[a,*], Xingye Chen[a], Michel Cathelinaud[b], Shuo Chen[a], Hongli Ma[b], Ping Fan[a], Xianghua Zhang[b], Zhenghua Su[a,*], Guangxing Liang[a,*]

[a]Shenzhen Key Laboratory of Advanced Thin Films and Applications Key Laboratory of Optoelectronic Devices and Systems, College of Physics and Optoelectronic Engineering, Shenzhen University, Shenzhen 518060, P. R. China.
E-mail: zhaojun@szu.edu.cn (Prof. Zhao), zhsu@szu.edu.cn (Prof. Su) and lgx@szu.edu.cn (Prof. Liang)

[b]CNRS, ISCR (Institut des Sciences Chimiques de Rennes), UMR 6226
Université de Rennes
Rennes F-35000, France

Supplementary Notes

Supplementary Note1 Bandgap calculation based on S/Se

The bandgap values of $Cu_2ZnSn(S_{1-x}Se_x)_4$ for different Se contents can be calculated using the sophisticated hybrid functional HSE (Heyd-Scuseria-Ernzerhof) reported by Chen et al. with the following formula:

$$E_g(x)=(1-x)E_g(\text{CZTS})+xE_g(\text{CZTSe})-bx(1-x) \qquad \text{(S1)}$$

where Se content is x, S content is 1-x, E_g(CZTS) is 1.5 eV, E_g(CZTSe) is 0.96 eV, and b denotes bandgap bending with a value of 0.07 eV[1].

Supplementary Note2 UPS analysis

The work function (φ) is obtained from the following equation:

$$\varphi = h\upsilon - E_{\text{cut off}} \qquad \text{(S2)}$$

where $h\upsilon$ is 21.22 eV (He I source) and $E_{\text{cut off}}$ is based on the extrapolation of the linear region of high binding energy[2].

Supplementary Note3 Calculation of CBO

The band alignment at the heterojunction contains both spike-type and cilff-type. When the electron affinity energy of the buffer layer is larger than that of the absorber, the CBO at the heterojunction is negative, and the band alignment at this time is cilff-type. The cilff-type band alignment will strongly increase the interface recombination and decrease the V_{OC}. And when the electron affinity energy of the buffer layer is smaller than that of the absorber, the CBO at the heterojunction is positive, and the band alignment is spike-type in this case. Spike-type band alignment is favorable to prevent electron return and reduce interface recombination, but excessive spike (too large CBO) affects the electron tunneling effect at the interface thus deteriorating the device performance. Relevant literatures show that CBO is optimal between 0-0.4 eV, in which the larger CBO is more favorable to reduce interface recombination. In this work, the CBO at the heterojunction of the With AS device is slightly increased due to the sulfurization treatment that improves the S/Se content in the near-surface region of the absorber layer, favoring the reduction of heterojunction interface recombination[3].

Supplementary Note4 KPFM analysis

KPFM is used to determine the electrostatic potential change between the probe and the sample due to the localized surface potential change. The brightness of the grain boundary (GB) of both samples is significantly higher than that of the grain interior (GI), and the potential difference between GI and GB can be expressed by the following equation:

$$\Delta \mathrm{CPD}=\varphi_{\mathrm{GI}}-\varphi_{\mathrm{GB}}=e\mathrm{V}_{\mathrm{CPD(GB)}}-e\mathrm{V}_{\mathrm{CPD(GI)}} \qquad \text{(S3)}$$

where φ_{GI} and φ_{GB} are the potentials at the GI and GB, respectively[4].

Supplementary Note5 Admittance spectra analysis

Admittance spectral measurements are used to estimate the defect level within the bandgap. The inflection frequency ω_0 of each admittance spectral curve is determined by the corner frequency point at the maximum of the $-\omega dC/d\omega$ plot (Figure S9). The fitting equation for the Arrhenius plot is[5]:

$$\omega_0 = 2\pi v_0 T^2 e^{-\frac{E_a}{kT}} \qquad \text{(S4)}$$

where ω_0 is the inflection frequency, E_a is the depth of the defect relative to the edge of the valence band, and v_0 is the exponential prefactor. In this case, the activation energy E_a determined from the Arrhenius diagram is approximated as the energy difference between the defect energy level and the valence band edge. The defect density obtained from the *C*-*f* scan is calculated as follows:

$$E_a = kTln(\frac{2\pi v_0 T^2}{\omega}) \qquad (S5)$$

$$N_T = -\frac{V_{bi}}{W_d} \cdot \frac{dC}{d\omega} \cdot \frac{\omega}{kT} \qquad (S6)$$

where N_T is the defect density, W_d is depletion width and V_{bi} is the built-in voltage[6].

Supplementary Note6 EIS analysis

EIS can be used to determine minority carrier (electron) recombination to characterize carrier transport behavior. The EIS data were fitted using an equivalent circuit model, which consists of a chemical capacitor (C_{rec}) connected by a shunt composite resistor (R_{rec}) and a series resistor (R_s*), and the measured carrier lifetimes corresponded to the carrier transport behavior within the absorber layer close to the CdS/CZTSSe interface. According to the diffusion-recombination model, the minority carrier lifetime can be calculated according to the following equation[7]:

$$\tau = R_{rec} \times C_{rec} \qquad (S7)$$

Supplementary Note7 *CV* and DLCP analysis

CV and DLCP are often used to analyze carrier concentration and depletion width in thin film solar cells. The formulas for the calculations are as follows[8]:

$$N_{CV} = \frac{C^3}{qA^2\varepsilon_0\varepsilon}\left(\frac{dC}{dV}\right)^{-1} \qquad (S8)$$

$$W_{d-CV} = \frac{\varepsilon_0\varepsilon A}{C} \qquad (S9)$$

$$N_{DL} = -\frac{C_0^3}{2q\varepsilon_0\varepsilon A^2 C_1} \qquad \text{(S10)}$$

$$W_{d-DL} = \frac{\varepsilon_0\varepsilon A}{C_0} \qquad \text{(S11)}$$

Where ε and ε_0 stand for the dielectric constant of the CZTSSe and vacuum dielectric constant, respectively; C, A and q is the measured capacitance, the active area of the cell, and elementary charge, C_0 and C_1 are two quadratic fitting parameters derived from the DLCP. Besides, The *CV* measurement is more sensitive to the interface state (N_{IT}) than the DLCP, so the interface state density can be obtained from the difference between the *CV* and the DLCP:

$$N_{\mathrm{IT}}=N_{\mathrm{CV}}-N_{\mathrm{DL}} \qquad \text{(S12)}$$

Supplementary Figures

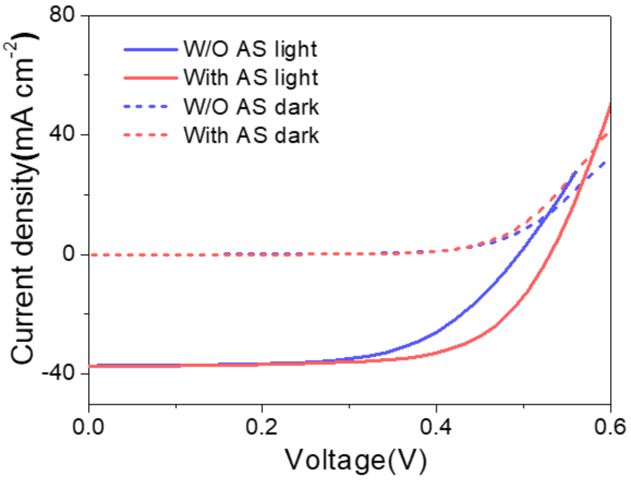

Figure S1 Light-state and dark-state *J*-*V* curves for W/O AS and With AS devices.

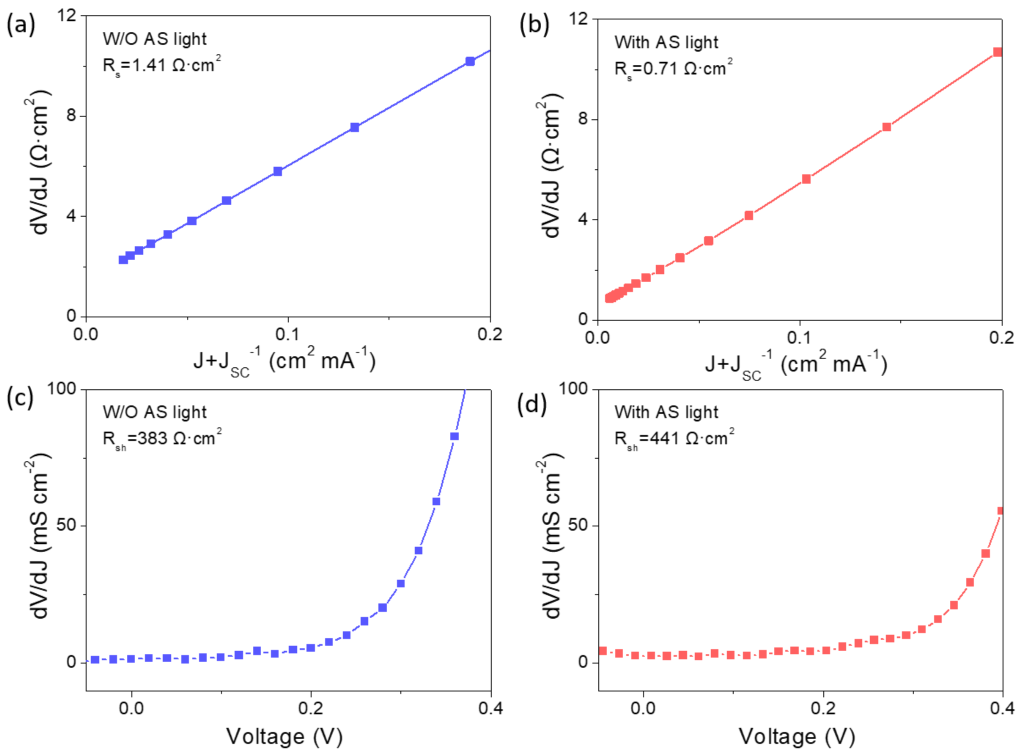

Figure S2 Series resistance (a, b) and parallel resistance (c, d) for W/O AS and With AS devices. (a) and (c) correspond to W/O AS device, (b) and (d) correspond to With AS device.

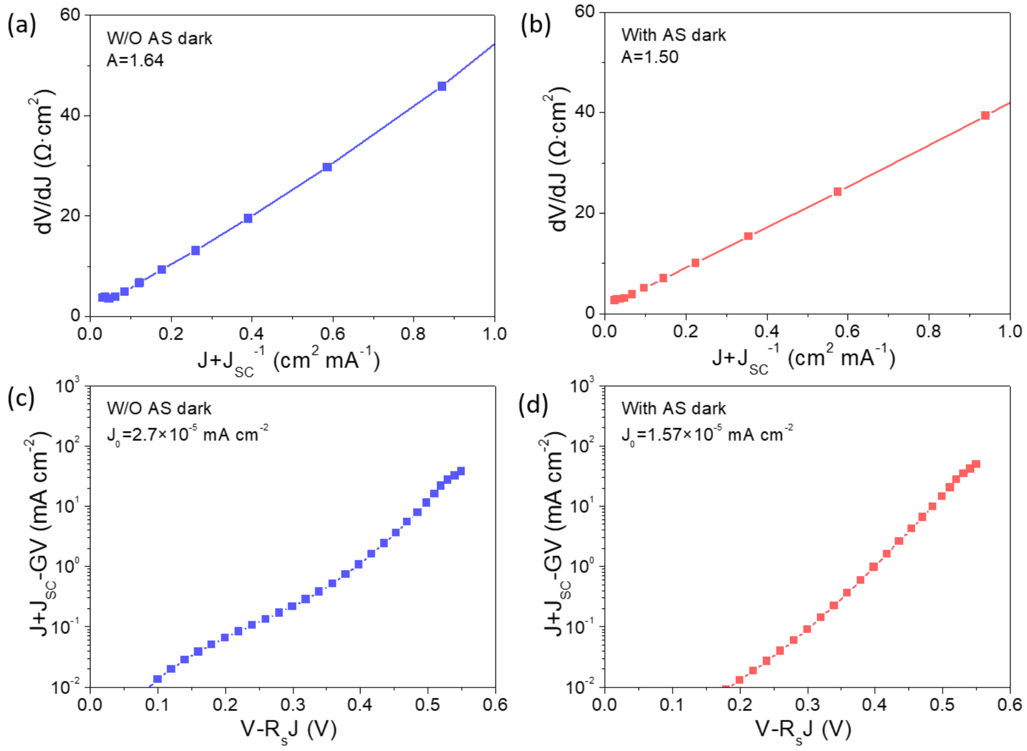

Figure S3 Diode ideal factor (a, b) and reverse saturation current (c, d) for W/O AS and With AS devices. (a) and (c) correspond to W/O AS devices, (b) and (d) correspond to With AS devices.

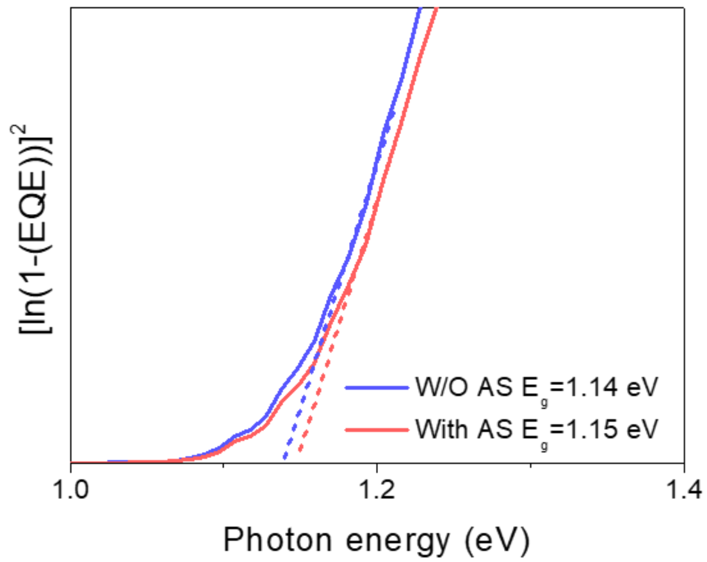

Figure S4 Bandgap of W/O AS and With AS devices calculated from EQE curves.

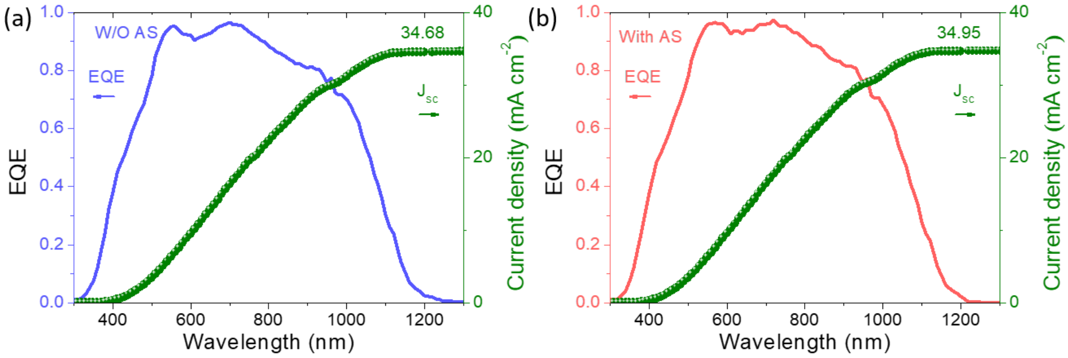

Figure S5 Integral current density of W/O AS (a) and With AS (b) devices calculated from EQE curve.

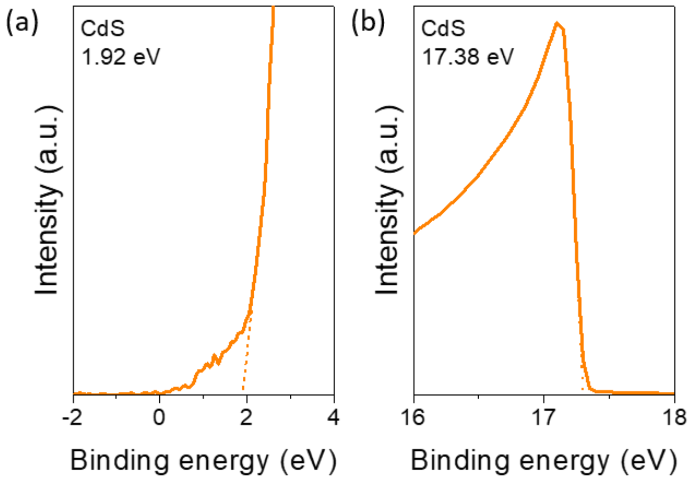

Figure S6 UPS curve for CdS. (a) correspond to low binding energy, (b) correspond to high binding energy.

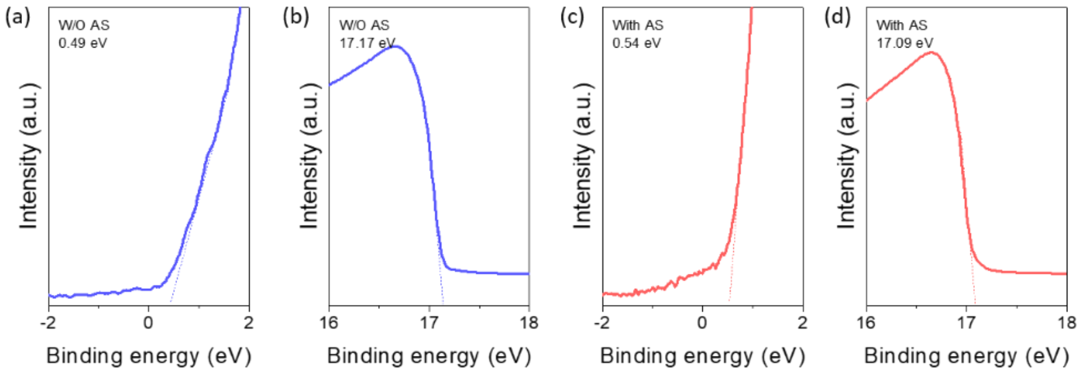

Figure S7 UPS curves for W/O AS (a, b) and With AS films (c, d). (a) and (c) correspond to low binding energy, (c) and (d) correspond to high binding energy.

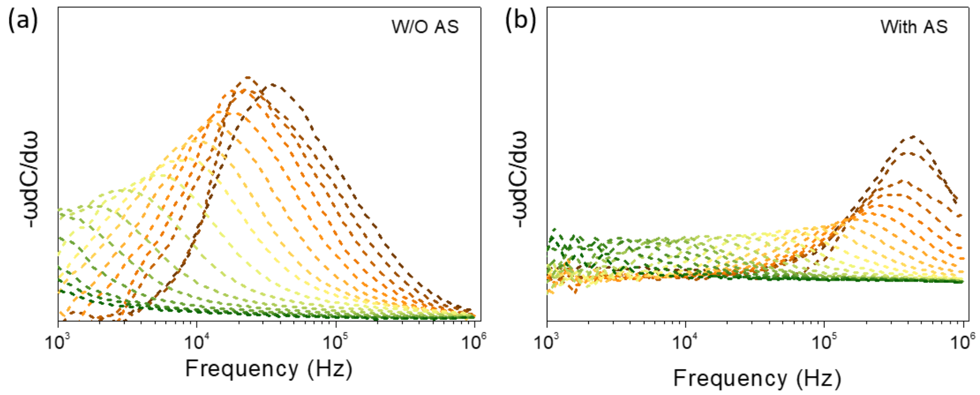

Figure S8 Plots of -$\omega \mathrm{d}C/\mathrm{d}\omega$ vs. frequency at different temperature for W/O AS (a) and With AS devices (b).

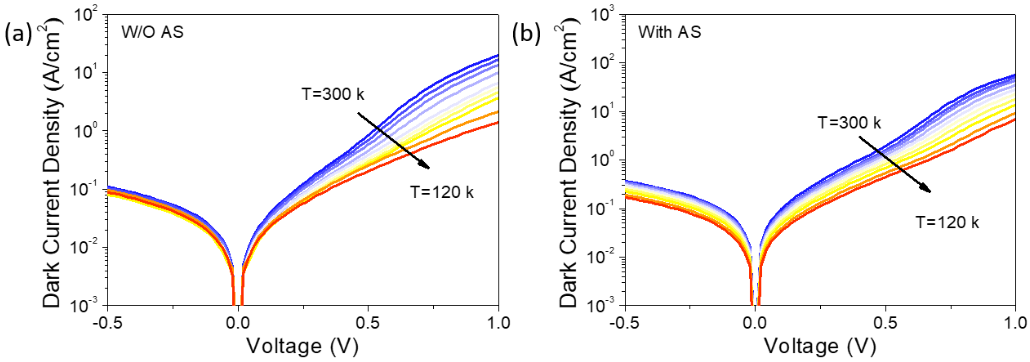

Figure S9 Temperature-dependent dark *J*–*V* curves of W/O AS device (a) and With AS device (b)

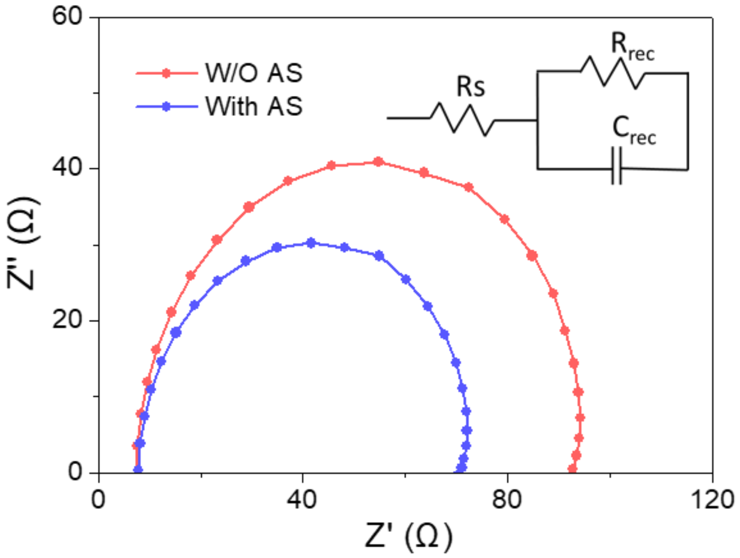

Figure S10 The EIS curves for the W/O AS and With AS devices, inset shows the equivalent circuit diagram.

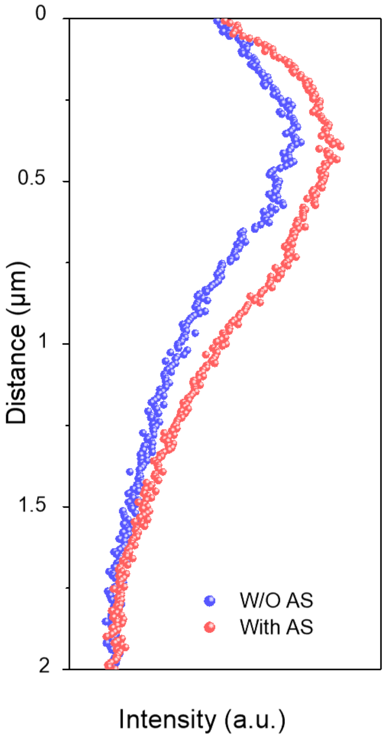

Figure S11 W/O AS and With AS device non-normalized EBIC signal line scanning.

Reference

[1] S. Chen, A. Walsh, J.-H. Yang, X.G. Gong, L. Sun, P.-X. Yang, J.-H. Chu, S.-H. Wei, Compositional dependence of structural and electronic properties of $Cu_2ZnSn(S,Se)_4$ alloys for thin film solar cells, Phys. Rev. B 83(12) (2011) 125201, https://doi.org/10.1103/PhysRevB.83.125201.

[2] Z. Yu, C. Li, S. Chen, Z. Zheng, P. Fan, Y. Li, M. Tan, C. Yan, X. Zhang, Z. Su, G. Liang, Unveiling the Selenization Reaction Mechanisms in Ambient Air‑Processed Highly Efficient Kesterite Solar Cells, Adv. Energy Mater. 13(19) (2023) 2300521, https://doi.org/10.1002/aenm.202300521.

[3] G.S. Park, V.B. Chu, B.W. Kim, D.W. Kim, H.S. Oh, Y.J. Hwang, B.K. Min, Achieving 14.4% Alcohol-Based Solution-Processed $Cu(In,Ga)(S,Se)_2$ Thin Film Solar Cell through Interface Engineering, ACS Appl. Mater. Interfaces 10(12) (2018) 9894-9899, https://doi.org/10.1021/acsami.8b00526.

[4] K. Kim, I. Jeong, Y. Cho, D. Shin, S. Song, S.K. Ahn, Y.-J. Eo, A. Cho, C. Jung, W. Jo, J.H. Kim, P.-P. Choi, J. Gwak, J.H. Yun, Mechanisms of extrinsic alkali incorporation in CIGS solar cells on flexible polyimide elucidated by nanoscale and quantitative analyses, Nano Energy 67 (2020) 104201, https://doi.org/10.1016/j.nanoen.2019.104201.

[5] H.-S. Duan, W. Yang, B. Bob, C.-J. Hsu, B. Lei, Y. Yang, The role of sulfur in solution-processed $Cu_2ZnSn(S,Se)_4$ and its Effect on defect properties, Adv. Funct. Mater. 23(11) (2013) 1466-1471, https://doi.org/10.1002/adfm.201201732.

[6] Y.-D. Luo, R. Tang, S. Chen, J.-G. Hu, Y.-K. Liu, Y.-F. Li, X.-S. Liu, Z.-H. Zheng, Z.-H. Su, X.-F. Ma, P. Fan, X.-H. Zhang, H.-L. Ma, Z.-G. Chen, G.-X. Liang, An effective combination reaction involved with sputtered and selenized Sb precursors for efficient Sb_2Se_3 thin film solar cells, Chem. Eng. J. 393 (2020) 124599, https://doi.org/10.1016/j.cej.2020.124599.

[7] Y.-R. Lin, V. Tunuguntla, S.-Y. Wei, W.-C. Chen, D. Wong, C.-H. Lai, L.-K. Liu, L.-C. Chen, K.-H. Chen, Bifacial sodium-incorporated treatments:Tailoring deep traps and enhancing carrier transport properties in Cu_2ZnSnS_4 solar cells, Nano Energy 16 (2015) 438-445, https://doi.org/10.1016/j.nanoen.2015.07.022.

[8] Y. Luo, G. Chen, S. Chen, N. Ahmad, M. Azam, Z. Zheng, Z. Su, M. Cathelinaud, H. Ma, Z. Chen, P. Fan, X. Zhang, G. Liang, Carrier Transport Enhancement Mechanism in Highly Efficient Antimony Selenide Thin‐Film Solar Cell, Adv. Funct. Mater. 33(14) (2023), https://doi.org/10.1002/adfm.202213941.